# Imaging of double slit interference by scanning gate microscopy

K. Kolasiński, B. Szafran, and M. P. Nowak

*AGH University of Science and Technology, Faculty of Physics and Applied Computer Science, al. A. Mickiewicza 30, 30-059 Krakow, Poland*

(Received 8 April 2014; revised manuscript received 26 August 2014; published 8 October 2014)

We consider scanning gate microscopy imaging of the double slit interference for a pair of quantum point contacts (QPCs) defined within the two-dimensional electron gas. The interference is clearly present in the scattered electron wave functions for each of the incident subbands. Nevertheless, we find that the interference is generally missing in the experimentally accessible conductance maps for many incident subbands. We explain this finding on the basis of the Landauer approach. A setup geometry allowing for observation of the double slit interference by scanning gate microscopy is proposed.

DOI: 10.1103/PhysRevB.90.165303 PACS number(s): 73.23.Ad, 73.63.Nm, 85.35.Ds

## I. INTRODUCTION

Interference effects for particles [1] are the cornerstone of quantum mechanical understanding of the wave nature of matter. The experiments including double slit interference were performed with electrons [2,3], ions [4], and larger objects including clusters and molecules [5]. The double slit interference implementing the Feynman version of the experiment was reported only very recently [6]. The interference experiments are performed on particles in vacuum [1–5] or in the solid state. The two-dimensional electron gas (2DEG) in semiconductor nanostructures is an attractive solid-state medium in this context due to a large coherence length for Fermi level electrons and carrier confinement that can be arbitrarily tailored for formation of electron interferometers [7]. The role of slits in 2DEG is played by quantum point contacts (QPCs) [8,9].

The electron flow determined by the Fermi level wave function is imaged by scanning gate microscopy (SGM) [10]. In the SGM technique the charged tip of the atomic force microscope locally perturbs the potential landscape within the 2DEG which is buried shallow beneath the surface of the semiconductor. The response of the system is monitored by conductance ($G$) maps as functions of the tip position. SGM was earlier used in quantum point contacts [11] for observation of the wave function diffraction including angular branching due to the conductance quantization inside the slit. The conductance maps contain interference patterns involving electron standing waves formed between the QPC and the tip [12]. SGM imaging of electron interferometers using antidots was also performed [13]. In spite of a large number of SGM studies of a single QPC [11,12,14] the imaging of the double slit interference was not reported so far. This paper investigates the problem of observation of the double slit interference by SGM.

We solve the phase coherent scattering problem for the Fermi level electron waves incident to the double slit system. The calculated SGM conductance map for the simplest double slit system does *not* contain signatures of the Young interference and is a sum of $G$ maps for separate slits. The double slit interference is present in the contributions to conductance for separate incident subbands but it disappears in the Landauer [15] summation. We explain this finding using symmetry arguments and indicate the setup geometry needed to obtain the interference signal in the SGM conductance map.

## II. THEORY

We consider a system depicted in Fig. 1(a) with a wide (500 nm) input lead and two open slits. We solve the coherent scattering problem as given by the Schrödinger equation for the Fermi level electrons. In order to determine the conductance we use a finite difference variant [16] of the quantum transmitting boundary method [17,18] for the effective mass Hamiltonian

$$H = -\frac{\hbar^2}{2m}\nabla^2 + V_{\rm con}(x,y) + V_{\rm tip}(x,y), \tag{1}$$

where $m = 0.067m_0$ is the GaAs electron effective mass, and $V_{\rm con}$ and $V_{\rm tip}$ are the potentials forming the confinement (a finite quantum well is applied) and describing the perturbation induced by the scanning tip, respectively. For the tip potential we use the Lorentz function as obtained in our previous Schrödinger-Poisson modeling [19],

$$V_{\rm tip}(x,y) = \frac{U_{\rm tip}}{1 + [(x-x_{\rm tip})^2 + (y-y_{\rm tip})^2]/d_{\rm tip}^2}, \tag{2}$$

where $(x_{\rm tip}, y_{\rm tip})$ is the position of the tip, $d_{\rm tip}$ is the width of the potential maximum, and $U_{\rm tip}$ its value.

In the input lead far from the QPCs the wave function is a superposition of incoming and backscattered waves

$$\Psi^{\rm input}(x,y) = \sum_{k=1}^{M} a_k e^{ikx}\chi_k^{\rm in}(y) + b_k e^{-ikx}\chi_{-k}^{\rm in}(y), \tag{3}$$

where the summation runs over wave vectors $k$ at the Fermi level. In the upper and lower ends of the computational box (the blue dashed lines in Fig. 1) transparent boundary conditions are applied [20], in form $\Psi(x, y \pm \Delta y) = \Psi(x,y)\exp(\pm i k_b \Delta y)$, where $k_b$ is an outgoing wave vector [20], $k_b = \sqrt{2mE_F/\hbar}$. In the output lead [black dashed vertical line in Fig. 1(a)] of width 1 $\mu$m we have the outgoing wave functions only:

$$\Psi^{\rm output}(x,y) = \sum_{k=1}^{M_{\rm out}} d_k e^{ikx}\chi_k^{\rm out}(y). \tag{4}$$

The transparent boundary conditions at the bottom and top boundaries and the outgoing boundary conditions at the output lead edge remove scattering from the ends of the computational box. In this paper we take $E_F = 6$ meV as the Fermi energy level for which we have $M = 16$ in the input lead. The edge of the computational box labeled as the output lead in Fig. 1(a) is

 

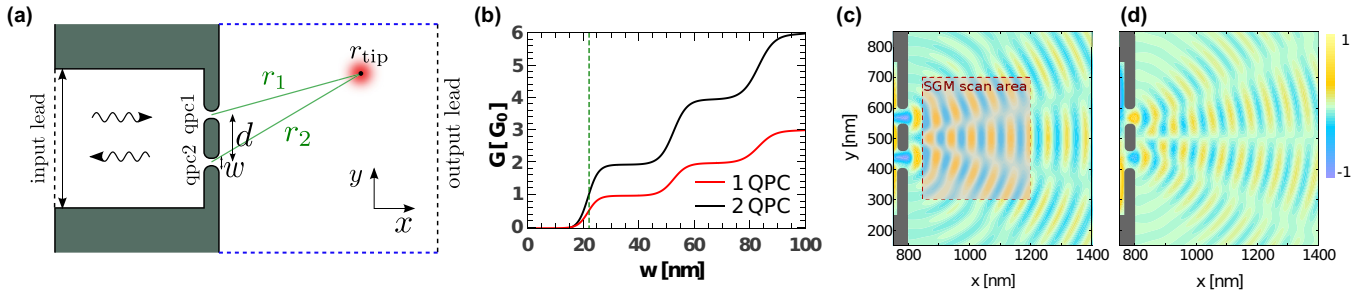


FIG. 1. (Color online) (a) Sketch of the double slit system for the electron incident from the left (lead of width 0.5 $\mu$m) with two QPCs of width $w$ with centers separated by $d = 130$ nm. The space at right of the slits is infinite with transparent boundary conditions [20] applied along the dashed lines [21]. $r_i$ is the distance between the $i$th QPC and the tip. (b) Conductance for a single (red line) and both (black line) QPCs open for Fermi energy $E_F = 6$ meV (16 conducting subbands in the input lead). (c) Real part of the wave function for the electron incident from the lowest (c) and second (d) subband.

treated as the channel of width 1 $\mu$m which at 6 meV carries $M_{\text{out}} = 32$ conducting subbands in the input and output leads, respectively. For the transparent and the outgoing boundary conditions the waves passed by QPC and the tip do not return to the discussed region upon reflection from the ends of the computational box. After solution of the scattering problem for each incoming mode the conductance of the system is evaluated by the Landauer formula $G = G_0 \sum_{i=1}^{M_{\text{in}}} T_i$, where $T_i$ is the transmission probability of the $i$th incoming mode and $G_0 = 2e^2/h$.

## III. RESULTS AND DISCUSSION

The calculated conductance for a single and two QPCs in the absence of the tip is plotted in Fig. 1(b) as a sum of contributions from 16 conducting subbands of the input lead. For further discussion we choose $w = 22$ nm at the first step of $G$: We shall discuss the simplest case of a single conducting subband for each QPC. The conductance maps obtained by the SGM for the QPC tuned to the $G$ steps exhibits oscillations with a high amplitude and radial fringes [12], which is convenient for discussion of the interference involving both slits. The real part of the wave functions is displayed in Figs. 1(c) and 1(d) for the transport calculated from the lowest and the second subband of opposite symmetry with respect to the lead axis.

The dashed rectangle of Fig. 1(c) indicates the area in which we will discuss the conductance maps obtained by SGM. The $G$ map calculated for a single QPC by the scattering problem with the method described in the previous section is displayed in Fig. 2(a). The map contains the radial fringes due to formation of the standing waves between the QPC and the tip. When both QPCs are open [Fig. 2(b)] we observe a checkerboard pattern which, however, turns out *not* to be the effect of the double slit wave function interference, as the pattern of the $G$ map can be exactly reproduced by the sum of $G$ maps for separate open slits [see Fig. 2(c)].

Let us explain the absence of the Young interference in the conductance maps. We begin by the case of a single QPC open. In the absence of the tip the wave function passing through the slit gets diffracted. The diffracted wave function can be quite well numerically simulated by the Huygens principle. Each point of the opening is a source of a circular wave and the resulting diffracted wave function can be calculated as

$$\Psi_{\text{QPC}}(\boldsymbol{r}) = \int_{\text{QPC}} d\mathbf{r}' f_{\text{QPC}}(y') \frac{e^{ik_F|r-r'|}}{\sqrt{|\mathbf{r}-\mathbf{r}'|}} \tag{5}$$

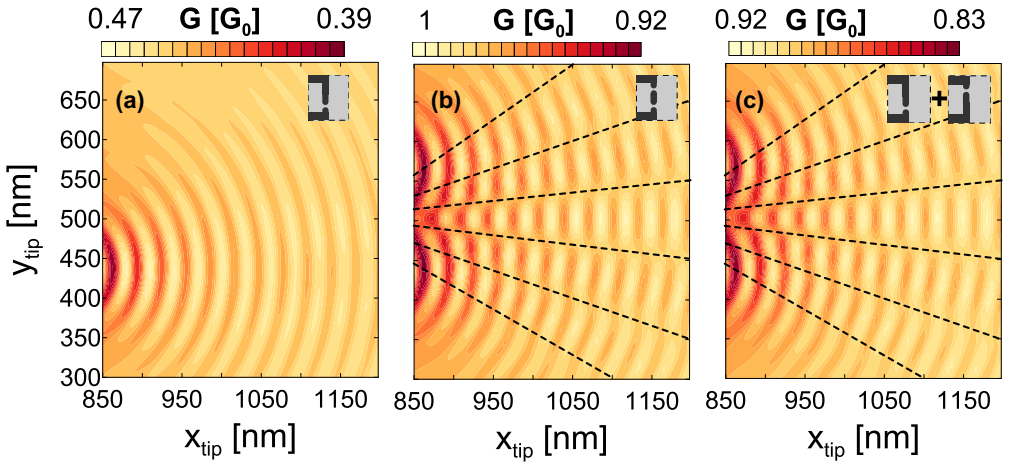


FIG. 2. (Color online) Conductance map for the QPC no. 2 open (a) and for both QPCs open (b). (c) Sum of conductance maps for separate QPCs open for tip potential parameters: $d_{\text{tip}} = 10$ nm and $U_{\text{tip}} = 5$ meV. The insets schematically explain the setup of the apparatus for each of the plots.

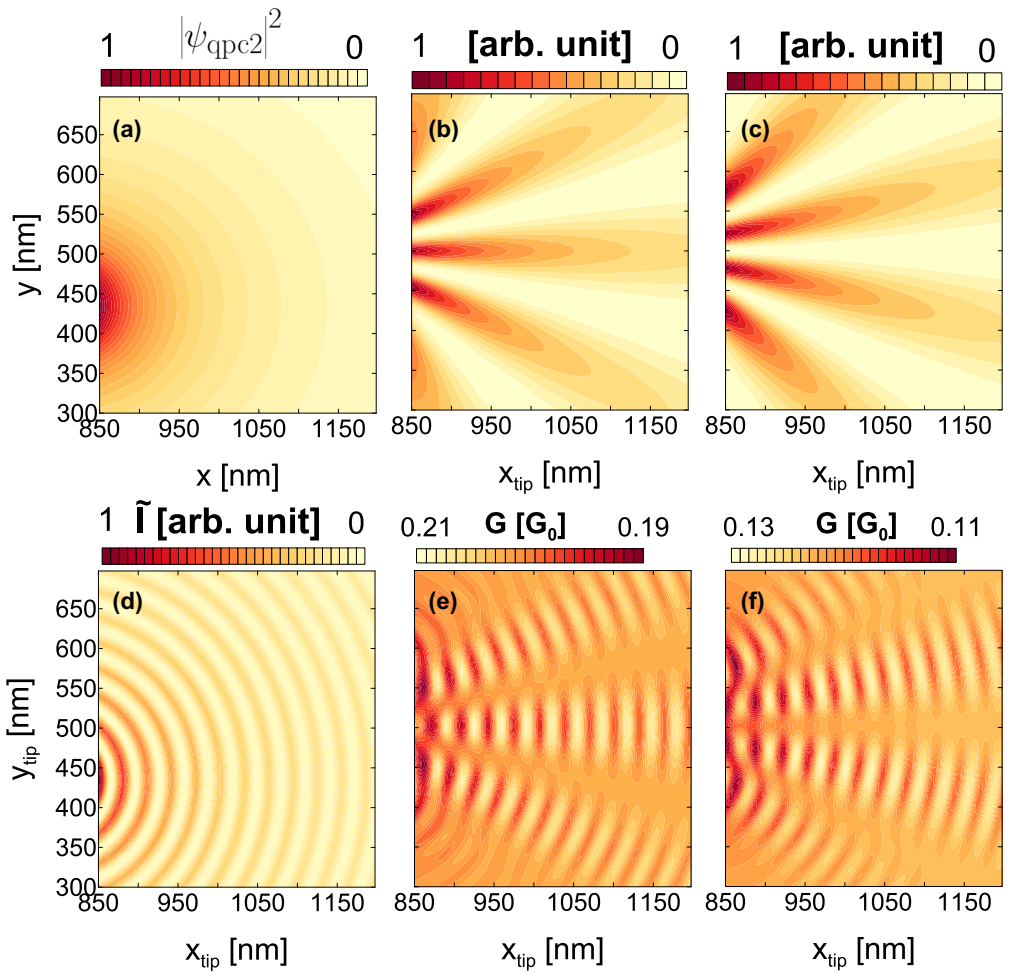


FIG. 3. (Color online) (a) Probability density for the diffracted wave function for the second QPC open in the absence of the tip as calculated from the scattering problem. (b) and (c) show the probability densities for interference of diffracted waves $|\Psi_1 \pm \Psi_2|^2$ with "+" in (b) and "−" in (c). (d) The variation of the probability density as given by Eq. (11) to be compared with the SGM map of Fig. 2(a). (e) and (f) show contributions to conductance in functions of the tip position for the lowest (e) and second (f) incident subband.

with the Fermi wave vector at the open half-space side ($\frac{\hbar^2 k_F^2}{2m} = E_F$) and the transverse wave function of the only conducting mode, which for the QPC center at the origin is $f_{\mathrm{QPC}}(y) = \sqrt{\frac{2}{w}}\sin(\frac{\pi y}{w})$ (for an infinite quantum well forming the constriction). The diffracted density calculated by Eq. (5) is displayed in Fig. 3(a). The diffracted wave function can be put in form

$$\Psi_l(\boldsymbol{r}) = \psi_{\mathrm{QPC}}(\mathbf{r})e^{ik_F r}, \tag{6}$$

where $\psi_{\mathrm{QPC}}$ is a slowly varying envelope function. When the tip is introduced to the system at position $\mathbf{r_{tip}}$ it gives rise to a scattering wave function $\Psi_{\mathrm{bs}}$ with the amplitude proportional to the envelope $\psi_{\mathrm{QPC}}$,

$$\Psi_{\mathrm{bs}}(\mathbf{r}) = R(\mathbf{r_{tip}} - \mathbf{r})\psi_{\mathrm{QPC}}(\mathbf{r})e^{ik_F|\mathbf{r_{tip}}-\mathbf{r}|}. \tag{7}$$

The $R$ function varies slowly as compared to the Fermi wavelength $2\pi/k_F$. Along the line between the tip and the QPC the superposition of the incoming [Eq. (6)] and backscattered [Eq. (7)] wave functions is approximately given by

$$\Phi(\mathbf{r}) = \psi_{\mathrm{QPC}}(\mathbf{r})\Phi_{\mathrm{bs}}(\mathbf{r}) \tag{8}$$

with

$$\Phi_{\mathrm{bs}} = (e^{ik_F r_l} + \alpha e^{-ik_F r_l}), \tag{9}$$

where a scattering amplitude $\alpha$ replaces $R$ function and $r_l$ stands for the distance to the $l$th slit [see Fig. 1(a)]. The SGM image is proportional to the probability density

$$\begin{aligned} I_{\mathrm{SGM}}(\mathbf{r}) &= |\Phi(\mathbf{r})|^2 = |\psi_{\mathrm{QPC}}(\mathbf{r})\Phi_{\mathrm{bs}}(\mathbf{r})|^2 \\ &= |\psi_{\mathrm{QPC}}(\mathbf{r})|^2\{|\alpha^2| + 1 + 2\Re(\alpha)[\cos^2(k_F r_l) - 1]\}. \end{aligned} \tag{10}$$

Neglecting the slowly varying terms the spatial variation of the probability density distribution is given by

$$\tilde{I}_{\mathrm{SGM}} = |\psi_{\mathrm{QPC}}(\mathbf{r})|^2\cos^2(k_F r_l). \tag{11}$$

Figure 3(d) shows $\tilde{I}_{\mathrm{SGM}}$ for the second QPC open which very well coincides with the variation of the exact conductance map of Fig. 2(a) with the oscillation period equal to half of the Fermi wavelength $\lambda_F/2 = 30$ nm.

The results of Fig. 2(b)—the $G$ map for both slits open—were calculated as a sum of contributions of 16 incident subbands given by separate scattering solutions (see the Theory section). The contribution of the incident subband $k$ to

the SGM image when both the slits are open is proportional to the probability density for the superposition of waves passing through one of the slits,

$$I_l(\boldsymbol{r}) = T_l|\psi_{\mathrm{QPC1}}(\boldsymbol{r})\Phi_{\mathrm{bs1}}(\boldsymbol{r}) \pm \psi_{\mathrm{QPC2}}(\boldsymbol{r})\Phi_{\mathrm{bs2}}(\boldsymbol{r})|^2, \quad (12)$$

where the sign $\pm$ depends on the parity of the incident mode $l$. The parity is $(-1)^{l+1}$, where $l$ numbers the energy subbands. For only two input channel subbands at the Fermi level the SGM image is given by

$$I_{\mathrm{SGM}} = I_1 + I_2 = (T_1 + T_2)(|\psi_{\mathrm{QPC1}}\phi_{\mathrm{bs1}}|^2 + |\psi_{\mathrm{QPC2}}\phi_{\mathrm{bs2}}|^2) + (T_1 - T_2)2\Re\{\psi_{\mathrm{QPC1}}\phi_{\mathrm{bs1}}\psi^*_{\mathrm{QPC2}}\phi^*_{\mathrm{bs2}}\},$$

which can be written as

$$I_{\mathrm{SGM}} = (T_1 + T_2)I_{\mathrm{no\,int}} + (T_1 - T_2)I_{\mathrm{int}}, \quad (13)$$

where $I_{\mathrm{no\,int}}$ is the sum of single slit images as given by Eq. (10), and the $I_{\mathrm{int}}$ is responsible for the interference effects. From the above formula it is clear that the interference signal vanishes when $T_1 \simeq T_2$. Figures 3(b) and 3(c) show the probability densities for the lowest and second incident subbands, calculated from wave function given by a sum and a difference of integrals of type (5), respectively. For the symmetry reasons in the lowest subband we have a central line of positive interference [Fig. 3(b)] for the lowest subband and a zero of the wave function for the second subband [Fig. 3(c)]. In Figs. 3(e) and 3(f) we plotted the $G$ maps obtained for the two subbands as calculated from the solution of the scattering problem. The maxima of the probability density coincide with the extrema of $G$ maps. The latter contains the interference fringes of the $\lambda_F/2$ period which correspond to standing waves between the tip and the QPC which were described above for a single QPC [cf. Figs. 2(a) and 3(d)].

Generalizing the description, for $M$ subbands in the input channel the SGM image is given as

$$I_{\mathrm{SGM}} = I_{\mathrm{no\,int}}T + I_{\mathrm{int}}\Delta_T, \quad (14)$$

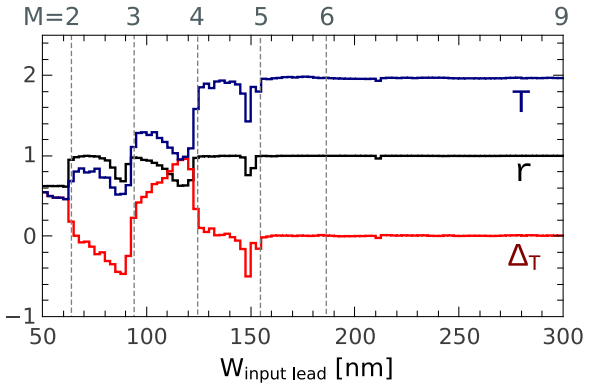


FIG. 4. (Color online) The number of incident subbands $M$ (top of the figure), the summed transfer probability $T$ [Eq. (15), blue line], and the value of $\Delta_T$ [Eq. (16)] as functions of the width of the input channel with fixed $E_F = 6$ meV. The black line ($r$) shows the correlation factor between the images of the probability density for both slit open, and the sum of densities for separate slits. The value of $r = 1$ indicates absence of the interference signal. The lower the value of $r$ the larger the interference features.

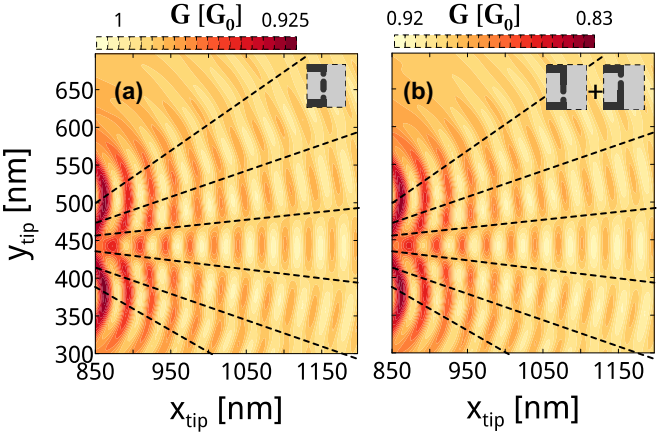


FIG. 5. (Color online) Same as Figs. 2(b) and 2(c) only for the QPCs shifted by 60 nm below the axis of the channel.

with

$$T = \sum_{i=1}^{M} T_i \quad (15)$$

and

$$\Delta_T = T_1 - T_2 + T_3 - T_4 + \cdots + T_{M-1} - T_M. \quad (16)$$

For the SGM image normalized to the summed transfer probability one obtains

$$\frac{I_{\mathrm{SGM}}}{T} = I_{\mathrm{no\,int}} + I_{\mathrm{int}}\frac{\Delta_T}{T}, \quad (17)$$

with the interference term vanishing for large $M$ since $\Delta_T \ll T$. This explains the result of Fig. 2, with the pattern of the $G$ map for the two QPCs [Fig. 2(b)] as a simple sum of maps for separate QPCs [Fig. 2(c)].

The disappearance of the interference signal with $M$ is described in a quantitative manner in Fig. 4. We keep $E_F = 6$ meV and vary the width of the input channel. The number of subbands $M$ is given on top of the figure. The summed transfer probability tends to $T = 2$ (each slit opens a single channel) for large $M$. The value of $\Delta_T$ vanishes for

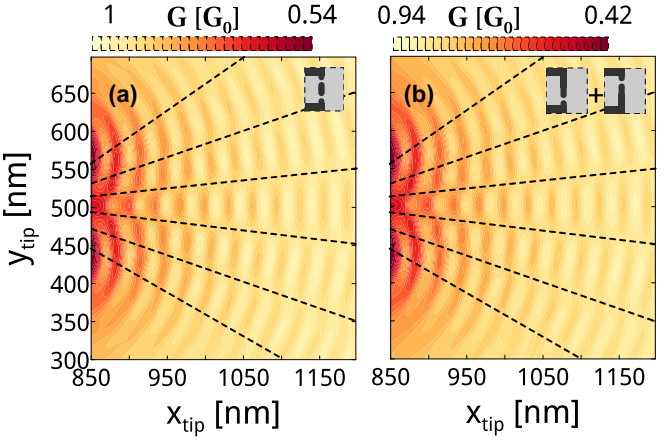


FIG. 6. (Color online) Same as Figs. 2(b) and 2(c) only for $U_{\mathrm{tip}}$ and $d_{\mathrm{tip}}$ increased twice, to 10 meV and 20 nm, respectively.

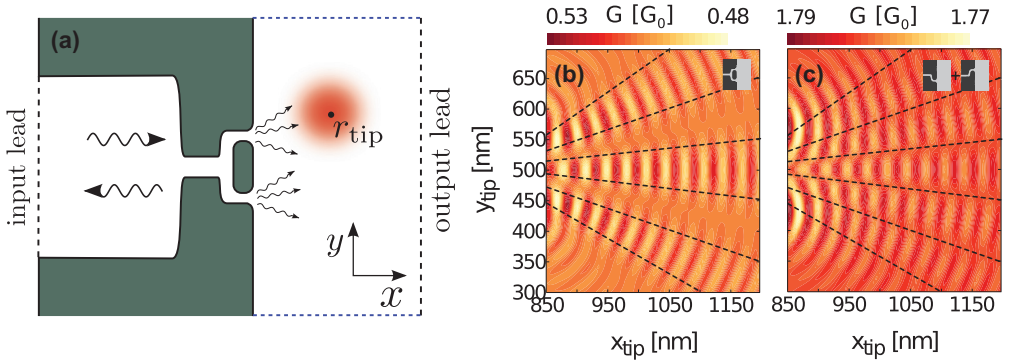


FIG. 7. (Color online) (a) Sketch of the system of double QPCs including a channel acting as the symmetry filter. The width of the channel is equal to the width of the opening $w = 22$ nm. (b) Conductance map for two QPCs open. (c) Sum of conductance maps of separate QPCs.

$M > 4$. For quantitative evaluation of the interference image we calculated the cross correlation coefficient $r$ [16] between (i) the scattering probability density for both slits open and (ii) the sum of densities for separate open slits (the black line in Fig. 4). The perfect correlation $r = 1$ corresponds to a complete absence of the interference features in the probability density map. The lower value of $r$ the more distinct are the interference features. We can see that for $M > 4$, $r$ becomes equal to 1 in consistence with the value of $\Delta_T$ tending to 0 [22]. Interference features are present for lower numbers of subbands, but only for $M = 1$ the value of $r$ does not depend on the width of the input channel.

Although the present interpretation is based on the symmetry of the incident eigenstates with respect to the axis of the input lead, we found that the absence of the Young interference is robust (see Fig. 5) against localization of the slits with respect to the axis. The present discussion of the interference effects is independent of the parameters of the tip potential. In Fig. 6 we present the conductance maps as obtained for the larger and wider tip potential with $d_{tip} = 20$ nm, $U_{tip} = 10$ meV, i.e., for both parameters increased twice as compared to the values used previously. The maps acquire a larger amplitude for the increased tip potential [cf. Figs. 2(b) and 2(c)], but $G$ for both slits open still has the pattern as given by a simple sum of maps for separate slits.

The above discussion indicates that the absence of the Young interference for many incident subbands results from cancellation of terms for various contributions to the total conductance in terms of the Landauer approach. The present finding of an absence of the interference in the case of several subbands is related to the suppression of the Aharonov-Bohm conductance oscillations with the period of the flux quantum [23]. Reference [23] indicated a reduction of the amplitude of the Aharonov-Bohm oscillation which decreases with the number of subbands as $1/M$. On the other hand, in the present work we demonstrated a complete *removal* of the interference effects already at $M = 5$.

A way to preserve a clear interference signal in the $G$ map is to filter out all the contributions but one. For that purpose we considered a channel of width $w = 22$ nm that feeds both the QPCs [see Fig. 7(a)]. The conductance maps calculated for both QPCs open and the 16 subbands incident in the input lead is given in Fig. 7(b). The horizontal channel has subbands on its own and at the Fermi energy it transmits current only in the lowest one. The total conductance map of Fig. 7(b) with the radial features and maxima collimated into three beams is similar to the one obtained above for the lowest subband contribution of Fig. 2(e). For comparison Fig. 7(c) shows the simple sum of $G$ maps obtained for a single QPC open with the checkerboard pattern encountered above in Fig. 2(b) before the filter channel was introduced.

## IV. SUMMARY AND CONCLUSIONS

We have discussed the SGM imaging of the Fermi level wave function interference with the conductance maps obtained by scanning gate microscopy. We solved the coherent scattering problem and demonstrated that although the double slit interference is present for each of the incident subbands separately, the signatures of the interference disappear when the total conductance is evaluated by the Landauer formula. We explained the absence of the double slit interference using symmetry arguments for the incident wave functions. A geometry in which the Young experiment can be performed by SGM was indicated.

## ACKNOWLEDGMENT

This work was supported by National Science Centre according to decision DEC-2012/05/B/ST3/03290, and by PL-Grid Infrastructure.

[1] C. Davisson and L. H. Germer, Nature (London) **119**, 558 (1927).
[2] C. Jönsson, Z. Phys. **161**, 454 (1961); Am. J. Phys. **42**, 4 (1974).
[3] F. Hasselbach, Rep. Prog. Phys. **73**, 016101 (2010).
[4] A. D. Cronin, J. Schmiedmayer, and D. E. Pritchard, Rev. Mod. Phys. **81**, 1051 (2009).
[5] K. Horbnerger, S. Gerlich, P. Haslinger, S. Nimmrichter, and M. Arndt, Rev. Mod. Phys. **84**, 157 (2012).

[6] R. Bach, D. Pope, S. H. Lou, and H. Batelaan, New J. Phys. **15**, 033018 (2013).

[7] B. I. Halperin, Phys. Rev. B **25**, 2185 (1982); B. W. Alphenaar, A. A. M. Staring, H. van Houten, M. A. A. Mabesoone, O. J. A. Buyk, and C. T. Foxon, *ibid.* **46**, 7236(R) (1992); B. J. van Wees, L. P. Kouwenhoven, C. J. P. M. Harmans, J. G. Williamson, C. E. Timmering, M. E. I. Broekaart, C. T. Foxon, and J. J. Harris, Phys. Rev. Lett. **62**, 2523 (1989); Y. Zhang, D. T. McClure, E. M. Levenson-Falk, C. M. Marcus, L. N. Pfeiffer, and K. W. West, Phys. Rev. B **79**, 241304(R) (2009); D. T. McClure, Y. Zhang, B. Rosenow, E. M. Levenson-Falk, C. M. Marcus, L. N. Pfeiffer, and K. W. West, Phys. Rev. Lett. **103**, 206806 (2009); B. Rosenow and B. I. Halperin, *ibid.* **98**, 106801 (2007); F. E. Camino, W. Zhou, and V. J. Goldman, *ibid.* **95**, 246802 (2005).

[8] A. Yacoby, M. Heiblum, V. Umansky, H. Shtrikman, and D. Mahalu, Phys. Rev. Lett. **73**, 3149 (1994).

[9] P. Khatua, B. Bansal, and D. Shahar, Phys. Rev. Lett. **112**, 010403 (2014).

[10] H. Sellier, B. Hackens, M. G. Pala, F. Martins, S. Baltazar, X. Wallart, L. Desplanque, V. Bayot, and S. Huant, Sem. Sci. Tech. **26**, 064008 (2011); D. K. Ferry, A. M. Burke, R. Akis, R. Brunner, T. E. Day, R. Meisels, F. Kuchar, J. P. Bird, and B. R. Bennett, *ibid.* **26**, 043001 (2011).

[11] R. Crook, C. G. Smith, M. Y. Simmons, and D. A. Ritchie, Phys. Rev. B **62**, 5174 (2000); M. A. Topinka, B. J. LeRoy, S. E. J. Shaw, E. J. Heller, R. M. Westervelt, K. D. Maranowski, and A. C. Gossard, Science **289**, 2323 (2000); M. A. Topinka, B. J. LeRoy, R. M. Westervelt, S. E. J. Shaw, R. Fleischmann, E. J. Heller, K. D. Maranowski, and A. C. Gossard, Nature (London) **410**, 183 (2001); N. Aoki, C. R. Da, C. R. Akis, D. K. Ferry, and Y. Ochiai, Appl. Phys. Lett. **87**, 223501 (2005); M. P. Jura, M. A. Topinka, L. Urban, A. Yazdani, H. Shtrikman, L. N. Pfeiffer, K. W. West, and D. Goldhaber-Gordon, Nat. Phys. **3**, 841 (2007); K. E. Aidala, R. E. Parott, T. Kramer, E. J. Heller, R. M. Westervelt, M. P. Hanson, and A. C. Gossard, *ibid.* **3**, 464 (2007); A. Kozikov, D. Weinmann, C. Rössler, T. Ihn, K. Ensslin, C. Reichl, and W. Wegscheider, New J. Phys. **15**, 083005 (2013).

[12] M. P. Jura, M. A. Topinka, M. Grobis, L. N. Pfeiffer, K. W. West, and D. Goldhaber-Gordon, Phys. Rev. B **80**, 041303(R) (2009).

[13] B. J. LeRoy, A. C. Bleszynski, K. E. Aidala, R. M. Westervelt, A. Kalben, E. J. Heller, S. E. J. Shaw, K. D. Maranowski, and A. C. Gossard, Phys. Rev. Lett. **94**, 126801 (2005); B. Hackens, F. Martins, S. Faniel, C. A. Dutu, H. Sellier, S. Huant, M. Pala, L. Desplanque, X. Wallart, and V. Bayot, Nat. Commun. **1**, 39 (2010); F. Martins, S. Faniel, B. Rosenow, M. G. Pala, H. Sellier, S. Huant, L. Desplanque, X. Wallart, V. Bayot, and B. Hackens, New J. Phys. **15**, 013049 (2013); F. Martins, S. Faniel, B. Rosenow, H. Sellier, S. Huant, M. G. Pala, L. Desplanque, X. Wallart, V. Bayot, and B. Hackens, Sci. Rep. **3**, 1416 (2013).

[14] For a theory of SGM on a single QPC, see, e.g., R. A. Jalabert, W. Szewc, S. Tomsovic, and D. Weinmann, Phys. Rev. Lett. **105**, 166802 (2010); C. Gorini, R. A. Jalabert, W. Szewc, S. Tomsovic, and D. Weinmann, Phys. Rev. B **88**, 035406 (2013).

[15] S. Datta, *Electronic Transport in Mesoscopic Systems* (Cambridge University Press, Cambridge, England, 1995).

[16] For the details of the method see K. Kolasiński and B. Szafran, Phys. Rev. B **89**, 165306 (2014).

[17] D. J. Kirkner and C. S. Lent, J. Appl. Phys. **67**, 6353 (1990).

[18] M. Leng and C. S. Lent, J. Appl. Phys. **76**, 2240 (1994).

[19] B. Szafran, Phys. Rev. B **84**, 075336 (2011); K. Kolasiński and B. Szafran, *ibid.* **88**, 165306 (2013).

[20] M. P. Nowak, K. Kolasiński, and B. Szafran, Phys. Rev. B **90**, 035301 (2014).

[21] The actual computational box at right of the QPCs is 1 $\mu$m by 1 $\mu$m.

[22] The values of transfer probability for separate subbands vary nonmonotonically with the width of the channel. For $W =$ 75 nm ($M = 2$) we find $T_1 = 0.34$, $T_2 = 0.47$ with $\Delta T = -0.13$; for $W = 110$ nm ($M = 3$) $T_1 = 0.025$, $T_2 = 0.23$, $T_3 = 0.92$, and $\Delta T = 0.715$; for $W = 140$ nm ($M = 4$) $T_1 = 0.078$, $T_2 = 0.25$, $T_3 = 0.89$, $T_4 = 0.68$, and $\Delta T = 0.038$; and for $W = 225$ nm ($M = 7$) $T_1 = 0.31$, $T_2 = 0.75$, $T_3 = 0.53$, $T_4 = 0.095$, $T_5 = 0.018$, $T_6 = 0.14$, $T_7 = 0.13$, and $\Delta T = 0.003$.

[23] M. Büttiker, Y. Imry, R. Landauer, and S. Pinhas, Phys. Rev. B **31**, 6207 (1985).